

# Self-interference 3D super-resolution microscopy for deep tissue investigations

Pierre Bon<sup>1,2\*</sup>, Jeanne Linarès-Loyez<sup>1,2</sup>, Maxime Feyeux<sup>1,2</sup>, Kevin Alessandri<sup>1,2</sup>, Brahim Lounis<sup>1,2</sup>, Pierre Nassoy<sup>1,2</sup> and Laurent Cognet<sup>1,2\*</sup>

**Fluorescence localization microscopy has achieved near-molecular resolution capable of revealing ultra-structures, with a broad range of applications, especially in cellular biology. However, it remains challenging to attain such resolution in three dimensions and inside biological tissues beyond the first cell layer. Here we introduce SELFI, a framework for 3D single-molecule localization within multicellular specimens and tissues. The approach relies on self-interference generated within the microscope's point spread function (PSF) to simultaneously encode equiphase and intensity fluorescence signals, which together provide the 3D position of an emitter. We combined SELFI with conventional localization microscopy to visualize F-actin 3D filament networks and reveal the spatial distribution of the transcription factor OCT4 in human induced pluripotent stem cells at depths up to 50  $\mu\text{m}$  inside uncleared tissue spheroids. SELFI paves the way to nanoscale investigations of native cellular processes in intact tissues.**

Single-molecule localization microscopy (SMLM)<sup>1–3</sup> allows scientists to study the structural complexity of biological samples at the molecular scale, including protein supramolecular assemblies and dynamic protein–protein interactions<sup>4–7</sup>. However, SMLM investigations in intact tissues, and thus observation of native 3D biological structures, remain challenging. Indeed, whereas 2D lateral super-localization is well established<sup>8</sup>, the recovery of localizations along the third dimension is currently limited to studies within isolated cells or the first cellular layer in multicellular samples, or to investigations of transformed tissue<sup>9,10</sup>. Optical aberrations that are introduced by the sample itself are the main obstacle to deep imaging at high resolution. The coupling of adaptive optics to SMLM can only partially overcome this limitation within the first micrometers of a sample<sup>11</sup>.

Several approaches have been described for determining the axial localization of single emitters. One of these approaches<sup>12,13</sup> imposes strict constraints on the sample, such as the presence of a coverslip near emitting fluorescent dipoles so that their distances from the glass surface can be measured. The penetration depth of this approach is thus limited to less than 1  $\mu\text{m}$  inside the sample. Another approach is based on multiple-plane or defocused imaging<sup>14–17</sup>. By registering one or a set of fluorescence images with different defocus values, one can retrieve the axial positions of emitters. A disadvantage of this method is the division of the total number of photons between the images, which deteriorates the localization precision. Another strategy uses  $4\pi$  interferometric microscopy to generate interferences on multiple detectors<sup>18</sup> and encode the axial positions of individual emitters. Although it is very precise, this technique remains a ‘tour de force’, which limits its widespread application. Moreover, the  $4\pi$  configuration is limited to thin samples. Finally, the most commonly used approach is based on engineering of the microscope's PSF<sup>19–25</sup>. The introduction of strong axial anisotropy to the PSF allows the user to extract the axial molecule positions. One drawback, however, is the substantial PSF enlargement, which may affect signal-to-noise ratios for the detection of single molecules. Moreover, the inherent sensitivity of

engineered PSFs to optical aberrations makes this approach ineffective beyond the first few micrometers inside a biological sample<sup>26</sup>.

Here we introduce SELFI, a 3D SMLM approach based on the generation of self-interferences within each detected PSF. SELFI is weakly sensitive to optical aberrations and thus allows 3D SMLM deep inside intact tissues. SELFI's principle relies on the fact that for a point source near the focal plane, the wavefront curvature of the fluorescence collected strongly depends on the axial position of the emitter (Supplementary Fig. 1) and exhibits a sign inversion at the focus. This is in contrast to the light intensity, which smoothly and symmetrically varies with the focus. In the imaging plane, analysis of the fluorescence wavefront (equiphase wave surfaces) through interferometry can therefore reveal the emitter's axial position. Because fluorescence is an incoherent process, external references cannot be used to generate the required interferences as in, for example, conventional holographic<sup>27,28</sup> or field scattering<sup>29,30</sup> methods. Self-interferences overcome this limitation, as they make it possible to manage the low spatiotemporal coherence of the fluorescence in an image plane. In a single camera frame, the axial super-localization is obtained by SELFI from the wavefront curvature, whereas the lateral localization is extracted from the intensity centroid.

## Results

**3D localization of single emitters by SELFI.** Because single-molecule luminescence signals are extremely weak, we designed a phase-only diffraction grating to be inserted a few micrometers in front of the microscope imaging plane (Fig. 1a) to generate self-coherent PSF replicas with >90% spatial overlap. We obtained interference patterns from 100-nm fluorescent nanobeads imaged in a wide-field configuration with different amounts of defocus (Fig. 1b and Supplementary Fig. 2). The interfringe varies with the emitter's axial position, whereas the envelope of the interference pattern directly corresponds to the PSF of the nonmodified microscope (i.e., without the diffraction grating). Two independent variables are thus obtained in a single image: the wavefront curvature given

<sup>1</sup>Université de Bordeaux, Laboratoire Photonique Numérique et Nanosciences, UMR 5298, F-33400 Talence, France. <sup>2</sup>CNRS and Institut d'Optique, LP2N UMR 5298, F-33400 Talence, France. \*e-mail: [pierre.bon@u-bordeaux.fr](mailto:pierre.bon@u-bordeaux.fr); [laurent.cognet@u-bordeaux.fr](mailto:laurent.cognet@u-bordeaux.fr)

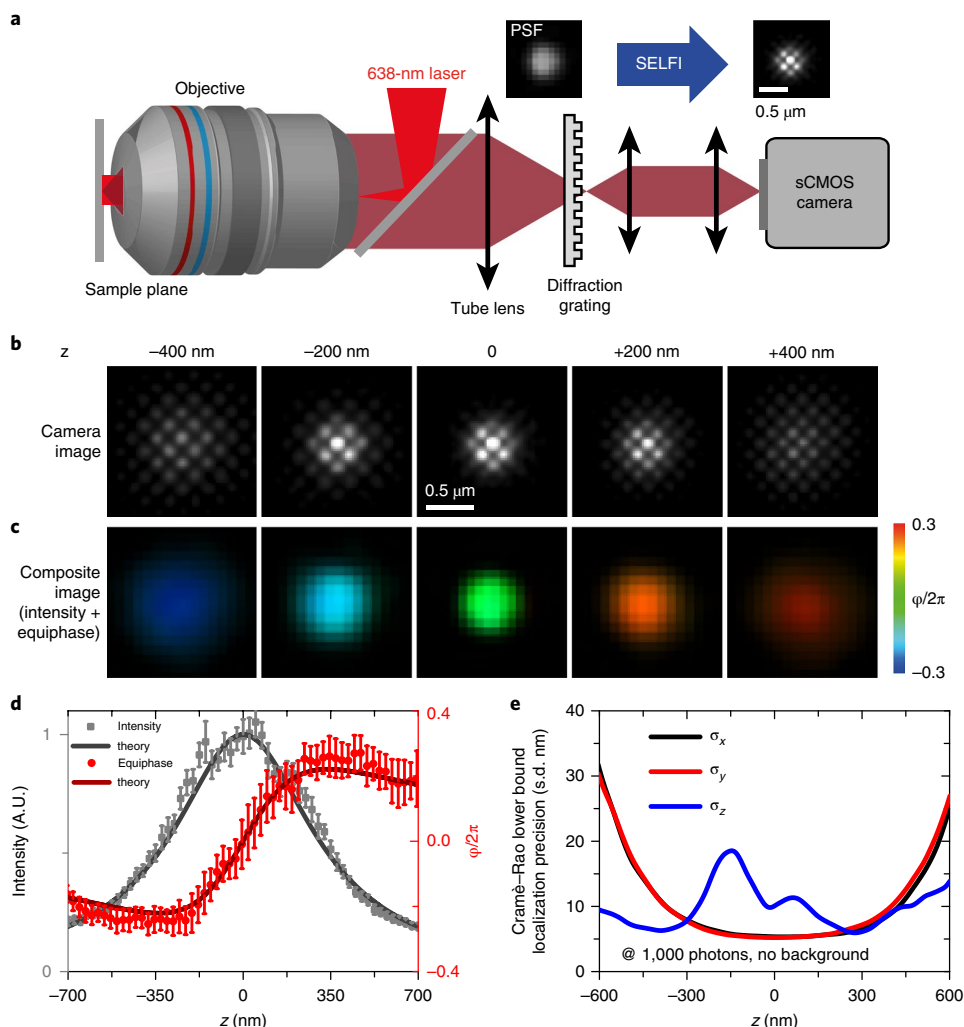


**Fig. 1 | Determination of the 3D localization of a single emitter by quantitative fluorescence intensity and equiphase imaging.** **a**, Schematic of the optical setup for fluorescence imaging. **b,c**, Interferograms (**b**) and intensity–phase composite images (**c**) (HSV color-coding, where H=phase, S=1 and V=intensity) of an unresolved 100-nm fluorescent bead (TetraSpeck) in focus ( $z=0$ ) or defocused within the depth of field ( $z=\pm 200$  or  $\pm 400$  nm). Note the sign inversion in the equiphase values after defocusing, in contrast to the intensity values. **d**, Intensity and equiphase signal variations of a single 100-nm fluorescent nanoparticle as a function of its axial position. The experimentally acquired values (dots and squares represent the average value of 10 acquisitions; error bars indicate s.d.) and the theoretical model (solid lines) are shown. A.U., arbitrary units. **e**, Localization precision obtained on the experimental data from **b** according to the Cramér–Rao lower bound. **b,c,e**, Representative values; similar results were obtained for all calibrations (total > 50) performed during this study.

by the interfringe, and the in-plane intensity distribution given by the envelope (Fig. 1c). We have developed an algorithm (Methods) that can extract the 3D position of the emitters from the interferogram with subwavelength precision. The experimentally measured intensity and phase dependence on the distance from the focus are both well reproduced with the theoretical model (Fig. 1d and Supplementary Note 1).

We assessed the experimental localization precision of SELFI according to the Cramér–Rao lower-bound approach<sup>31,32</sup>. The axial precision and its dependence on the distance from the focus are directly linked to the position of the grating with respect to the imaging plane, in the same manner as in the cylindrical lens PSF-shaping approach<sup>20,32</sup>. We found that the lateral precision of localization remained unchanged compared with that for a standard 2D SMLM setup (i.e., without diffraction grating; for example,  $\sigma_{xy} \sim 6$  nm for 1,000 detected photons from an in-focus emitter; Fig. 1e and Supplementary Fig. 3), which confirmed that self-interference does not broaden the PSF envelope. In addition, although the SELFI PSF

is oversampled to record the interferences, the bright fringes primarily contain the useful information for lateral localization, which leads to negligible degradation of precision compared with that in conventional 2D SMLM. Furthermore, owing to the high sensitivity of interferometry, SELFI is quasi-isotropic, as the axial precision of the localization is comparable to the lateral precision over the whole depth of field (Fig. 1e).

We experimentally compared SELFI to astigmatic PSF shaping, the most commonly used 3D super-localization technique (using a cylindrical lens; Fig. 2a and Supplementary Note 2). Although the lateral localization precision was comparable for the two approaches, SELFI showed substantially better axial localization precision. We then quantified the localization precision and accuracy for deep super-resolution imaging (Fig. 2b,c). To mimic tissue studies, we acquired images at various depths in a phantom composed of fluorescent nanobeads embedded in agarose gel. Astigmatic PSF shaping became inaccurate beyond a depth of 10  $\mu\text{m}$ : optical aberrations impaired the signal carrying the axial information. This led

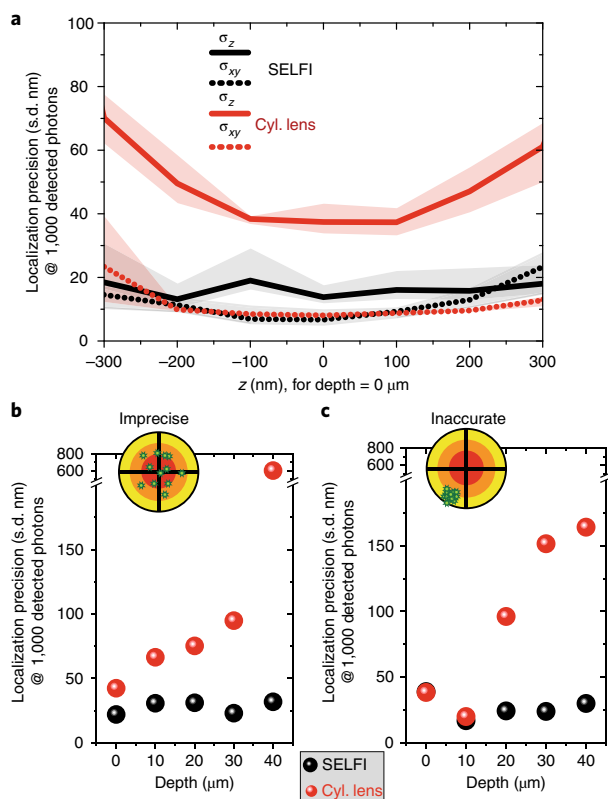


**Fig. 2 | Experimental localization precision and accuracy for the SELFI approach compared with that for PSF-shaping with a cylindrical lens.** **a**, Localization precision for ( $x$ ,  $y$ ) (dotted lines) and  $z$  (solid lines) obtained for different axial positions of the fluorescent nanobead emitter at depth 0 in the sample. Curves represent the average localization s.d. at each depth, and shaded areas represent the s.d. of the localization s.d. (200 replicates per depth). **b**, Localization precision at different depths within the sample. **c**, Localization accuracy at different depths within the sample. **a–c**, Black, SELFI; red, PSF-shaping.

to incorrect localization even with a high number of collected photons per molecule. In contrast, SELFI remained precise and accurate over several tens of micrometers: as long as a single-molecule image was formed on the camera (i.e., ballistic photons were collected), the light curvature was measurable. In other words, whenever 2D super-localization is possible, the axial localization can be determined by SELFI. For optimal accuracy of the measured axial super-localization, a calibration should be performed (Methods) in the presence of approximately the same amount of spherical aberration as in the foreseen application, which is predictable for in-depth biological imaging<sup>33</sup>.

**3D super-resolution imaging of F-actin network in cultured cells.** We next applied SELFI to direct stochastic optical reconstruction microscopy (dSTORM)<sup>34</sup>. We imaged fixed adherent human fibroblast cells (WI-38) in which the F-actin network was stained with phalloidin–Alexa Fluor 647 (Fig. 3). We reconstructed the 3D image from  $26 \times 10^6$  detected molecules (Fig. 3c, Supplementary Fig. 4 and Supplementary Video 1). The 3D super-localization was reconstructed within the depth of field of the microscope objective, and the F-actin subnetwork was clearly resolved compared with that in the diffraction-limited fluorescence image (Fig. 3a). This demonstrates that SELFI can handle densely labeled molecular structures such as the F-actin network, owing to its nonspeaking PSF. Indeed, for 3D dSTORM of F-actin, a high density of detected molecules is necessary, which imposes both a long dark state of the blinking fluorophores and a PSF as sharp as possible to avoid cross-talk between single-molecule subimages. SELFI can also be used to record label-free phase images under white-light trans-illumination via application of the quadriwave lateral shearing interferometry algorithm<sup>35,36</sup>. In this case, the quantitative phase image is linked to the optical path difference introduced by the sample (Figs. 3b and 4b,g). Acquisition of the label-free image can take place before, after or interleaved with fluorescence imaging. It can thus be used to identify a region of interest before or during fluorescence SMLM imaging and to get a bleaching-free reference of the cell morphology, which is useful given the long acquisition and computational times required by SMLM techniques.

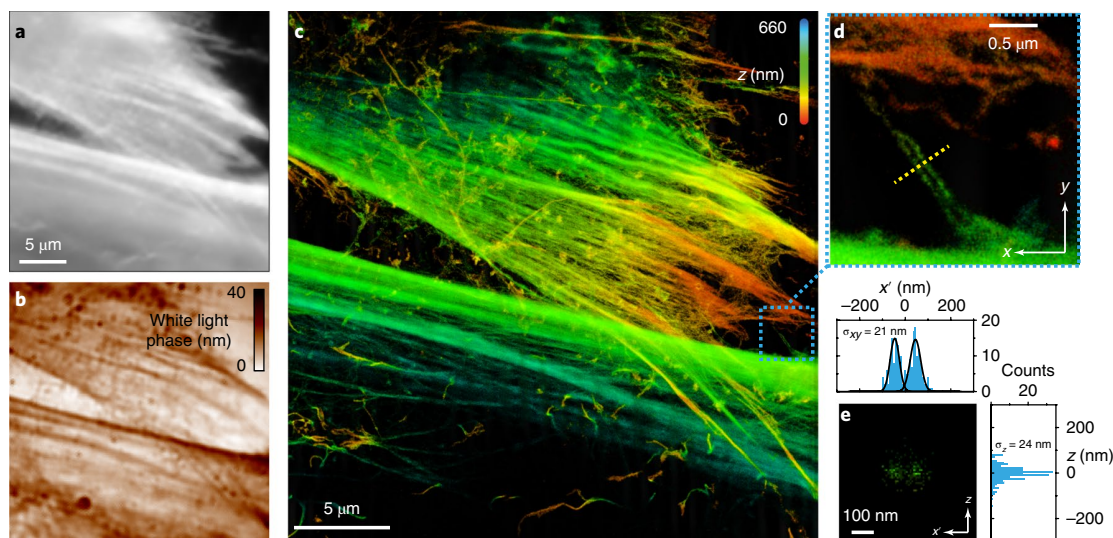


**Fig. 3 | Super-resolution imaging of F-actin in fixed adherent cells.** **a**, Epi-fluorescence image. Scale bar also applies to **b**. **b**, Label-free quantitative phase image obtained with the same setup as for **a**. **c**, F-actin super-resolution image of the same zone as in **b**, considering detection with at least 1,500 photons. **d**, A zoomed-in view of the region outlined by the dashed blue rectangle in **c**, showing two quasi-parallel F-actin fibers. **e**, Line-out of the region indicated by the dashed yellow line in **d** and projected histograms along  $x'$  (top) and  $z$  (right), showing quasi-isotropic resolution. The experiment was repeated on five different samples; representative results for a single sample are shown.

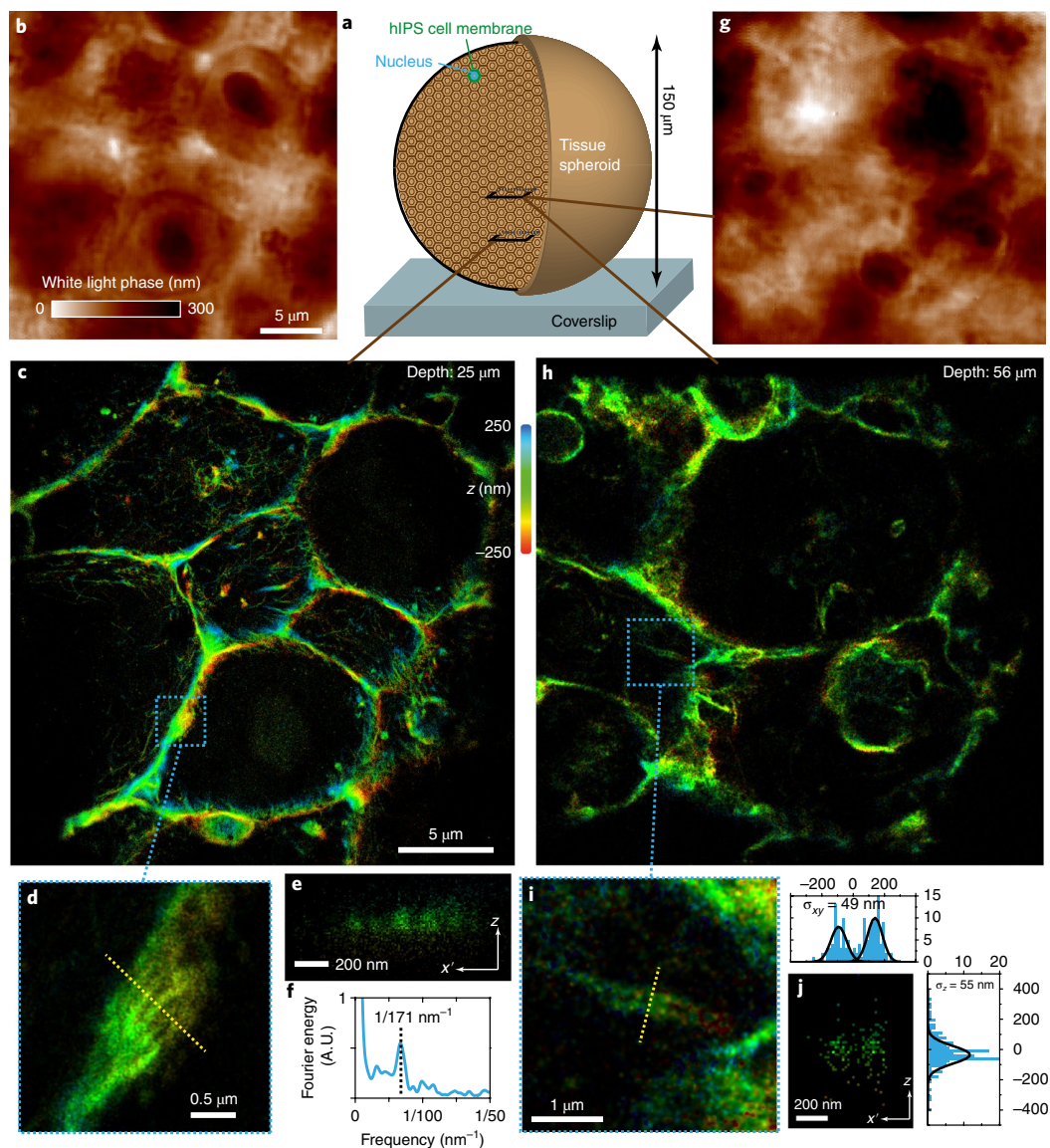


**Fig. 4 | Super-resolution imaging of F-actin in fixed thick samples.** **a**, Schematic of the spheroid sample with the imaging planes represented. **b**, Label-free quantitative phase imaging at 25  $\mu\text{m}$ . Scale bar also applies to **g**. **c**, F-actin super-resolution image of the same zone as in **b**, considering detection with at least 1,000 photons ( $1.6 \times 10^6$  detected molecules). Scale bar also applies to **h**. **d**, Zoomed-in view of the region outlined by the dashed blue rectangle in **c**, showing periodic F-actin fibers. **e**, Line-out of the region indicated by the yellow dashed line in **d**. **f**, Fourier transform spectrum of the region in **e**, showing a periodicity of 171 nm. **g**, Label-free quantitative phase image at 56  $\mu\text{m}$ . **h**, F-actin super-resolution image of the same zone as in **g**, considering detection with at least 500 photons ( $0.5 \times 10^6$  detected molecules). **i**, Zoomed-in view of the region outlined by the dashed blue rectangle in **h**, showing two parallel F-actin fibers. **j**, Line-out of the region indicated by the yellow dashed line in **i** and projected histograms along  $x'$  (top) and  $z$  (right), showing quasi-isotropic resolution. The experiment was repeated on six spheroids; representative data from a single sample are shown.

We next assessed the 3D resolution of SELFI-dSTORM by analyzing individualized unresolved F-actin fibers. We obtained a resolution of  $\sigma_{x,y,z}^{\text{fit}}$  of (21; 21; 24) nm (Fig. 3c,d) by Gaussian fitting of the detection distributions. This is equivalent to a full-width at half-maximum resolution (Rayleigh criterion) of  $R_{x,y,z}^{\text{fit}} = (49; 49; 56)$  nm. A more robust way to determine the actual resolution is to use the Fourier ring correlation (FRC) approach<sup>37</sup>. We obtained an FRC resolution  $R_{x,y,z}^{\text{FRC}}$  of (40; 40; 49) nm. The two approaches led to comparable results: the 3D resolution was quasi-isotropic for phalloidin-based F-actin labeling. Furthermore, this confirms again that the lateral resolution obtained is not degraded by the diffraction grating, as similar lateral resolution has been obtained in 2D dSTORM F-actin fiber reconstruction<sup>37</sup>.

**Deep 3D super-resolution imaging within tissue.** Next, we demonstrated 3D super-resolution at depth (Fig. 4a). We imaged F-actin fibers with dSTORM at 25  $\mu\text{m}$  (Fig. 4b–f) and 56  $\mu\text{m}$  (Fig. 4g–j) within 150- $\mu\text{m}$ -thick tissue spheroids derived from human induced pluripotent stem (hIPS) cells. Notably, we carried out the experiments with samples that were not subjected to a clearing protocol. Organoids of stem cells are increasingly considered as important models for both fundamental biology and regenerative medicine applications<sup>38,39</sup>. Axial stacks of 2D super-resolution images have already been reported for spheroids<sup>40</sup>, but to our knowledge 3D super-resolution imaging in uncleared samples has been limited to the first micrometers above a coverslip. Here we considered spheroids at their final

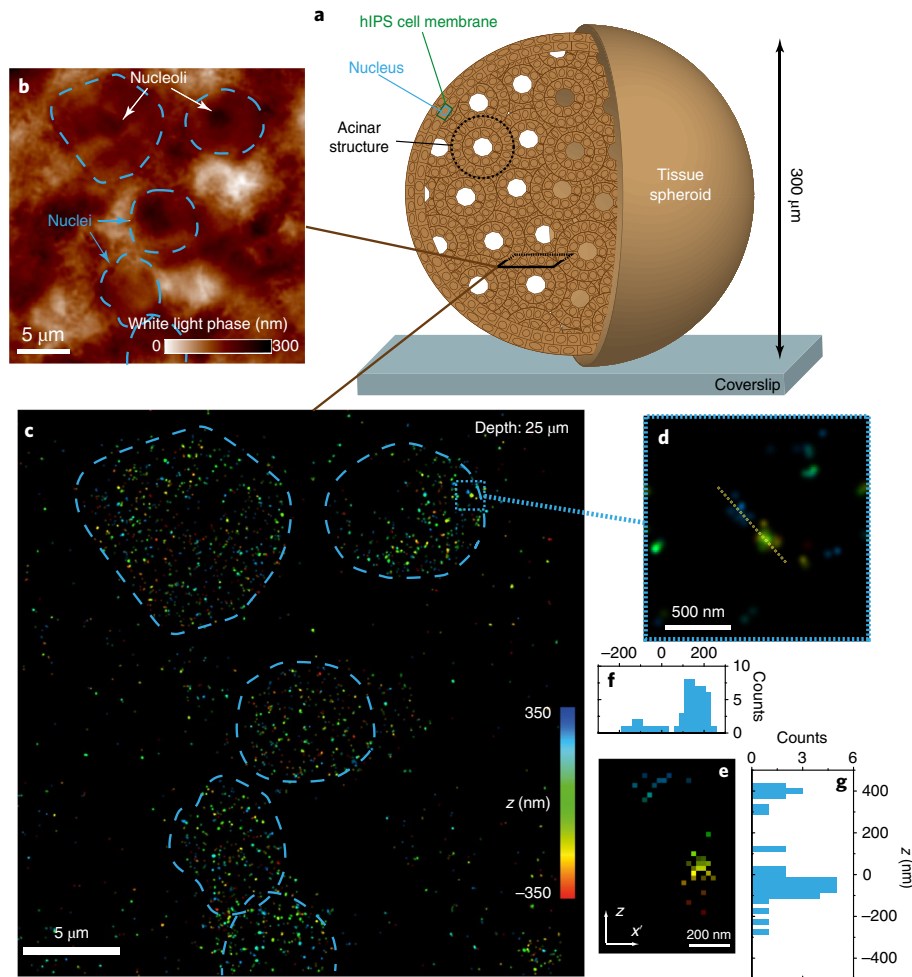


**Fig. 5 | Super-resolution imaging of OCT4 in fixed inhomogeneous thick samples.** **a**, Schematic of the spheroid sample with the imaging plane represented. **b**, Label-free quantitative phase imaging at 25  $\mu\text{m}$ . **c**, Super-resolution image of OCT4 in the same zone shown in **b**, considering detection with at least 1,500 photons (7,000 detected molecules). **d**, Zoomed-in view of the region outlined by the blue dashed rectangle in **c**, showing two clusters of molecules. **e**, Line-out of the region indicated by the yellow dashed line in **d**. **f**, Projected histogram along  $x'$  in **e**. **g**, Projected histogram along  $z$  in **e**. The experiment was repeated on six spheroids; representative data from a single sample are shown.

developmental stage, at which they have homogeneous but dense cell structures. In addition to super-resolution images, we also obtained white-light quantitative phase images from the same fields of view (Fig. 4b,g). SELFI super-resolved images (Fig. 4c,h) revealed subdiffraction structures: at 25  $\mu\text{m}$ , F-actin fibers with a period of 171 nm were unambiguously resolved (Fig. 4d–f). We further observed that F-actin structures appeared dense near the plasma membranes in a 3D tissue with both radial and orthoradial filaments. We then determined the 3D resolution in tissue: we obtained a quasi-isotropic resolution  $R_{x,y,z}^{\text{FRC}}$  of (61; 61; 66) nm at 25- $\mu\text{m}$  depth in the sample when considering molecules detected with at least 1,000 photons. At a depth of 56  $\mu\text{m}$ , the 3D super-resolution  $R_{x,y,z}^{\text{fit}}$  was (115; 115; 129) nm and  $R_{x,y,z}^{\text{FRC}}$  was (103; 103; 117) nm for molecules with at least 500 detected photons. As expected, the resolution for deeper imaging was lower than that for shallower imaging, primarily because of light scattering, which both decreases the number of ballistic photons and increases fluorescence background.

We next considered 3D super-resolution imaging of endogenous proteins in organoids by using secondary antibody immunostaining (Fig. 5). More precisely, we focused on imaging OCT4, a transcription factor expressed in hIPS cells. The expression of

four transcription factor genes (*NANOG*, *POU5F1* (*OCT4*), *KLF4* and *SOX2*) is sufficient to induce pluripotency in adult human fibroblasts<sup>41,42</sup>. We imaged in 300- $\mu\text{m}$  tissue spheroids displaying multiple acinar-like structures (Fig. 5a). These structures at this early developmental stage are reminiscent of the acinar structures present in a variety of organs. The samples were thus highly inhomogeneous (and optically aberrant), displaying properties analogous to those of genuine tissues. 3D super-resolved images obtained at 25  $\mu\text{m}$  inside the organoids showed that in hIPS cells, OCT4 proteins are homogeneously distributed within the nuclei and are excluded from nucleoli, which we identified by quantitative phase imaging (Fig. 5b–g). Under the same imaging conditions, we could not reconstruct a realistic 3D super-resolution image with astigmatic PSF-shaping (Supplementary Fig. 5 and Supplementary Note 3). Finally, at 25  $\mu\text{m}$  inside the sample, we measured an  $R_{x,y,z}^{\text{FRC}}$  value of (68  $\pm$  20; 68  $\pm$  20; 115  $\pm$  32) nm (mean  $\pm$  s.d.) for molecules near the imaging plane and  $R_{x,y,z}^{\text{FRC}}$  of (82  $\pm$  25; 82  $\pm$  25; 49  $\pm$  18) nm for molecules detected 400 nm above the imaging plane. We note that because of the limited number of detected OCT4 molecules compared with that for F-actin imaging (Fig. 4), SELFI resolution for the OCT4 images was determined with greater uncertainty (Fig. 5).

## Discussion

SELI unlocks 3D super-resolution deep within intact tissue. It does not require active optical corrections (e.g., adaptive optics) or cleared samples. Thanks to its intrinsic instrumental simplicity, we expect that it can be coupled with other microscopy techniques such as selective plane illumination (e.g., (lattice) light-sheet microscopy<sup>40,43</sup>) to reject out-of-focus fluorescence background, thereby enhancing the 3D super-resolution capability for imaging within tissue. As SELFI is based on wave-curvature sensing (which is an achromatic quantity), it should be suitable for sequential multicolor super-resolution imaging. Moreover, SELFI should also be valuable for investigations in living biological samples, including 3D tracking of fluorescently labeled submicrometer structures (e.g., molecules, vesicles or other organelles) with nanoscale precision deep within tissue.

## Methods

Methods, including statements of data availability and any associated accession codes and references, are available at <https://doi.org/10.1038/s41592-018-0005-3>.

Received: 23 October 2017; Accepted: 27 February 2018;

Published online: 30 April 2018

## References

- Betzig, E. et al. Imaging intracellular fluorescent proteins at nanometer resolution. *Science* **313**, 1642–1645 (2006).
- Rust, M. J., Bates, M. & Zhuang, X. Sub-diffraction-limit imaging by stochastic optical reconstruction microscopy (STORM). *Nat. Methods* **3**, 793–795 (2006).
- Sharonov, A. & Hochstrasser, R. M. Wide-field subdiffraction imaging by accumulated binding of diffusing probes. *Proc. Natl. Acad. Sci. USA* **103**, 18911–18916 (2006).
- Dani, A., Huang, B., Bergan, J., Dulac, C. & Zhuang, X. Superresolution imaging of chemical synapses in the brain. *Neuron* **68**, 843–856 (2010).
- Kanchanawong, P. et al. Nanoscale architecture of integrin-based cell adhesions. *Nature* **468**, 580–584 (2010).
- Rossier, O. et al. Integrins  $\beta 1$  and  $\beta 3$  exhibit distinct dynamic nanoscale organizations inside focal adhesions. *Nat. Cell Biol.* **14**, 1057–1067 (2012).
- Winckler, P. et al. Identification and super-resolution imaging of ligand-activated receptor dimers in live cells. *Sci. Rep.* **3**, 2387 (2013).
- Yildiz, A. et al. Myosin V walks hand-over-hand: single fluorophore imaging with 1.5-nm localization. *Science* **300**, 2061–2065 (2003).
- Chen, F., Tillberg, P. W. & Boyden, E. S. Expansion microscopy. *Science* **347**, 543–548 (2015).
- Richardson, D. S. & Lichtman, J. W. Clarifying tissue clearing. *Cell* **162**, 246–257 (2015).
- Ji, N. Adaptive optical fluorescence microscopy. *Nat. Methods* **14**, 374–380 (2017).
- Franke, C., Sauer, M. & van de Linde, S. Photometry unlocks 3D information from 2D localization microscopy data. *Nat. Methods* **14**, 41–44 (2017).
- Bourg, N. et al. Direct optical nanoscopy with axially localized detection. *Nat. Photonics* **9**, 587–593 (2015).
- Rosen, J. & Brooker, G. Non-scanning motionless fluorescence three-dimensional holographic microscopy. *Nat. Photonics* **2**, 190–195 (2008).
- Ram, S., Prabhat, P., Chao, J., Ward, E. S. & Ober, R. J. High accuracy 3D quantum dot tracking with multifocal plane microscopy for the study of fast intracellular dynamics in live cells. *Biophys. J.* **95**, 6025–6043 (2008).
- Abrahamsson, S. et al. Fast multicolor 3D imaging using aberration-corrected multifocus microscopy. *Nat. Methods* **10**, 60–63 (2013).
- Geissbuehler, S. et al. Live-cell multiplane three-dimensional super-resolution optical fluctuation imaging. *Nat. Commun.* **5**, 5830 (2014).
- Shtengel, G. et al. Interferometric fluorescent super-resolution microscopy resolves 3D cellular ultrastructure. *Proc. Natl. Acad. Sci. USA* **106**, 3125–3130 (2009).
- Kao, H. P. & Verkman, A. S. Tracking of single fluorescent particles in three dimensions: use of cylindrical optics to encode particle position. *Biophys. J.* **67**, 1291–1300 (1994).
- Huang, B., Wang, W., Bates, M. & Zhuang, X. Three-dimensional super-resolution imaging by stochastic optical reconstruction microscopy. *Science* **319**, 810–813 (2008).
- Pavani, S. R. P. & Piestun, R. Three dimensional tracking of fluorescent microparticles using a photon-limited double-helix response system. *Opt. Express* **16**, 22048–22057 (2008).
- Jia, S., Vaughan, J. C. & Zhuang, X. Isotropic 3D super-resolution imaging with a self-bending point spread function. *Nat. Photonics* **8**, 302–306 (2014).
- Roider, C., Jesacher, A., Bernet, S. & Ritsch-Marte, M. Axial super-localisation using rotating point spread functions shaped by polarisation-dependent phase modulation. *Opt. Express* **22**, 4029–4037 (2014).
- Backer, A. S., Backlund, M. P., von Diezmann, A. R., Sahl, S. J. & Moerner, W. E. A bisected pupil for studying single-molecule orientational dynamics and its application to three-dimensional super-resolution microscopy. *Appl. Phys. Lett.* **104**, 193701 (2014).
- Shechtman, Y., Weiss, L. E., Backer, A. S., Lee, M. Y. & Moerner, W. E. Multicolour localization microscopy by point-spread-function engineering. *Nat. Photonics* **10**, 590–594 (2016).
- McGorty, R., Schnitzbauer, J., Zhang, W. & Huang, B. Correction of depth-dependent aberrations in 3D single-molecule localization and super-resolution microscopy. *Opt. Lett.* **39**, 275–278 (2014).
- Cuche, E., Marquet, P. & Depeursinge, C. Simultaneous amplitude-contrast and quantitative phase-contrast microscopy by numerical reconstruction of Fresnel off-axis holograms. *Appl. Opt.* **38**, 6994–7001 (1999).
- Suck, S. Y., Collin, S., Bardou, N., De Wilde, Y. & Tessier, G. Imaging the three-dimensional scattering pattern of plasmonic nanodisk chains by digital heterodyne holography. *Opt. Lett.* **36**, 849–851 (2011).
- Piliarik, M. & Sandoghdar, V. Direct optical sensing of single unlabelled proteins and super-resolution imaging of their binding sites. *Nat. Commun.* **5**, 4495 (2014).
- Allier, C. et al. Imaging of dense cell cultures by multiwavelength lens-free video microscopy. *Cytometry A* **91**, 433–442 (2017).
- Ober, R. J., Ram, S. & Ward, E. S. Localization accuracy in single-molecule microscopy. *Biophys. J.* **86**, 1185–1200 (2004).
- Badieirostami, M., Lew, M. D., Thompson, M. A. & Moerner, W. E. Three-dimensional localization precision of the double-helix point spread function versus astigmatism and biplane. *Appl. Phys. Lett.* **97**, 161103 (2010).
- Booth, M. J., Neil, M. A. A. & Wilson, T. Aberration correction for confocal imaging in refractive-index-mismatched media. *J. Microsc.* **192**, 90–98 (1998).
- van de Linde, S. et al. Direct stochastic optical reconstruction microscopy with standard fluorescent probes. *Nat. Protoc.* **6**, 991–1009 (2011).
- Bon, P., Maucort, G., Wattellier, B. & Monneret, S. Quadriwave lateral shearing interferometry for quantitative phase microscopy of living cells. *Opt. Express* **17**, 13080–13094 (2009).
- Bon, P., Monneret, S. & Wattellier, B. Noniterative boundary-artifact-free wavefront reconstruction from its derivatives. *Appl. Opt.* **51**, 5698–5704 (2012).
- Nieuwenhuizen, R. P. et al. Measuring image resolution in optical nanoscopy. *Nat. Methods* **10**, 557–562 (2013).
- Clevers, H. Modeling development and disease with organoids. *Cell* **165**, 1586–1597 (2016).
- McCauley, H. A. & Wells, J. M. Pluripotent stem cell-derived organoids: using principles of developmental biology to grow human tissues in a dish. *Development* **144**, 958–962 (2017).
- Cella Zanacchi, F. et al. Live-cell 3D super-resolution imaging in thick biological samples. *Nat. Methods* **8**, 1047–1049 (2011).
- Takahashi, K. et al. Induction of pluripotent stem cells from adult human fibroblasts by defined factors. *Cell* **131**, 861–872 (2007).
- Yu, J. et al. Induced pluripotent stem cell lines derived from human somatic cells. *Science* **318**, 1917–1920 (2007).
- Legant, W. R. et al. High-density three-dimensional localization microscopy across large volumes. *Nat. Methods* **13**, 359–365 (2016).

## Acknowledgements

We thank C. Malrieux for help with tissue preparation, E. Fort and S. L ev eque-Fort for fruitful discussions, and L. Groc and J. Ferreira (Univ. Bordeaux, Interdisciplinary Institute for Neuroscience, CNRS UMR 5297, Bordeaux, France) for anti-IgG–Alexa Fluor 647. This work was supported by CNRS (to P.N.), the Agence Nationale de la Recherche (ANR-14-OHRI-0001-01 and ANR-15-CE16-0004-03 to L.C.), IdEx Bordeaux (ANR-10-IDEX-03-02 to L.C.), the France-BioImaging national infrastructure (ANR-10-INBS-04-01 to L.C. and B.L.) and Conseil Regional Nouvelle-Aquitaine (2015-1R60301-00005204 to L.C.).

## Author contributions

P.B., B.L. and L.C. conceived the study; P.B. designed the optical system; P.B. and L.C. supervised the study; K.A., M.F. and P.N. designed and produced the organoid tissues; P.B. and J.L.-L. prepared the samples for dSTORM and performed experiments and data analysis; and P.B., B.L. and L.C. wrote the manuscript. All authors discussed the data and agreed on the final manuscript.

## Competing interests

The authors declare no competing interests.

## Additional information

Supplementary information is available for this paper at <https://doi.org/10.1038/s41592-018-0005-3>.

Reprints and permissions information is available at [www.nature.com/reprints](http://www.nature.com/reprints).

Correspondence and requests for materials should be addressed to P.B. or L.C.

**Publisher's note:** Springer Nature remains neutral with regard to jurisdictional claims in published maps and institutional affiliations.

## Methods

**Optical setup.** All measurements were performed on a commercial inverted microscope (TiE; Nikon) equipped with a 60×/1.3-NA (numerical aperture) silicon objective (Olympus) and a double-stage filter set to allow simultaneous imaging of Alexa Fluor 647 fluorophores and transmission light at  $\lambda = 561 \pm 10$  nm for 3D drift correction<sup>44</sup> (see below). Fluorophores are excited by a 638-nm laser diode (HL63193; Oclaro) in a wide-field epi-configuration while the transmission white light is emitted by a halogen lamp (Nikon) filtered at  $561 \pm 10$  nm (Semrock), distinct from the excitation and emission fluorescence bands. The fluorescence detection path is composed of a phase-only diffraction grating inserted close to the imaging plane of the microscope output port and optically relayed by a dual-doublet telescope on an sCMOS (scientific complementary metal-oxide semiconductor) sensor (Orca Flash 4; Hamamatsu). The diffraction grating design is described below. For 3D dSTORM, images are recorded with an integration time of 30 ms per frame. The total acquisition time depends on the observed structures and the density of labeling; it varies between 15 min (Fig. 5) for molecular imaging of endogenous proteins with limited copy numbers and 8 h (Fig. 3) for dense structures such as F-actin filaments.

**Drift compensation.** To compensate for drift during the acquisition, 3D stabilization of the microscope is applied, using transmission light intensity and phase imaging with a commercial quadriwave lateral shearing interferometer<sup>35,45</sup> (SID4-element; Phasics) coupled with an sCMOS camera (Orca Flash 4; Hamamatsu) as described previously<sup>44</sup>. A sample structure providing high white-light quantitative phase imaging contrast (typically a vesicle) is actively kept at the focus while lateral drifts are corrected in post-processing during the super-resolution image reconstruction. This approach works not only near a coverslip but also in a thick sample. The drift compensation is performed at 40 Hz.

**Diffraction grating.** We use a custom-designed phase-only diffraction grating etched in fused silica. The structure consists of  $(0; \pi)$ -shift periodic switching forming a chessboard pattern with a period  $P$  of 20  $\mu\text{m}$  (Supplementary Fig. 1). The  $\pi$ -shift suppresses the nondiffracted light by destructive interference. The grating is placed a few micrometers away from the imaging plane of the microscope (equivalent to a few nanometers in the sample space), and the microscope imaging plane is optically relayed by the 4*f* imaging system on the camera (Fig. 1).

**Software and algorithm for image acquisition, single-emitter superlocalization and image reconstruction.** All custom-made programs were coded in the Labview environment (National Instruments), from the acquisition of the raw interferograms to the 3D image reconstruction and analysis. For single-emitter 3D localization retrieval from the raw PSF interferograms, the algorithm consists in (i) extracting the intensity image by low-pass filtering to perform lateral superlocalization by 2D Gaussian fitting based on the Levenberg–Marquardt algorithm<sup>46</sup>, and (ii) determining the emitter axial position by comparison (Pearson coefficient) of the measured Fourier transform PSF with a lookup table of  $z$ -dependent Fourier transform PSFs (see below).

**Lookup table for determination of axial localization.** To determine the axial position of a single fluorescent molecule, one needs to generate a calibration lookup table based on bright PSFs in different imaging planes, as is commonly done for 3D single-molecule localization. For this, we used fluorescent nanobeads (100-nm TetraSpeck; Thermo Fisher) deposited on a regular 1.5-type coverslip. We moved the microscope objective along the  $z$  direction in steps of 25 nm, using the microscope stepping-motor to record the SELFI PSF with different amounts of defocus (Fig. 1b). For super-resolution in tissue, the calibration is done at the coverslip with the objective collar optimized for  $z=0$  depth and then tuned to its optimized position for the considered imaging depth. This ensures a nearly identical amount of spherical aberration between the calibration and the measurements.

**Preparation of dSTORM samples. Fibroblast cells.** Human fibroblast cells (WI-38; passages 10–20; Coriell Institute) were grown in DMEM supplemented with 10% FBS, 1% L-glutamine and 1% penicillin–streptomycin (Life Technologies, USA) in a humidified cell culture incubator (37 °C and 5% CO<sub>2</sub>). After several days, cells were plated at low confluency on coverslips.

**Human induced pluripotent stem cell culture.** The BC-1 (WT XY; passages 15–25; MTI-Globalstem, USA) hIPS cell line was maintained under feeder-free conditions. Culture plates were coated with Matrigel matrix (Corning; 354248; 1/100 in DMEM for 2 h at 37 °C). BC-1 colonies were routinely subcultured with the enzyme-free cell-dissociation buffer ReLeSR (05873; Stemcell Technologies).

The pluripotent stem cells were cultured in mTESR1 (85850; Stemcell Technologies) complemented with 1% penicillin–streptomycin (Invitrogen). Cultures were fed daily and passaged every 5–7 d.

**Encapsulation and cyst development of hIPS cells.** The BC-1 (WT XY; passages 15–25; MTI-Globalstem, USA) hIPS cells were detached with ReLeSR (05873; Stemcell Technologies), resuspended at  $2 \times 10^6$  cells per mL in sorbitol solution and mixed (1:1) with Matrigel. For further details concerning the encapsulation procedure, please refer to the study by Alessandri et al.<sup>47</sup>.

When cultured in the presence of Matrigel, hIPS cells form cysts that grow in size until mechanical forces spontaneously reorganize them into multiple acinar-like structures (Fig. 5), then transition into a rather homogeneous structure (Fig. 4) and ultimately trigger cell death.

**Fixation, staining and mounting.** For F-actin imaging, we applied a fixation and staining step according to the protocol described by Xu et al.<sup>48</sup>. Briefly, fixation was done with 2% glutaraldehyde with 0.25% Triton X (Sigma-Aldrich) in so-called cytoskeleton buffer (3 mM MgCl<sub>2</sub>, 20 g/l KCl, 0.76 g/l EGTA, 3.9 g/l MES in pure water). Staining was carried out overnight with phalloidin–Alexa Fluor 647 (A22287; Thermo Fisher) diluted in 1% BSA.

For OCT4 imaging, 4% PFA fixation was performed, followed by permeabilization with 1% saponin for 30 min. OCT4 immunostaining was then carried out (A24867; Molecular Probes). First a rabbit anti-human OCT4 antibody diluted in 3% BSA was incubated for 3 h at room temperature. The sample was then washed four times for 15 min each time in PBS, and a secondary goat anti-rabbit IgG antibody coupled with Alexa Fluor 647 (A21245; Thermo Fisher) was added, diluted in 3% BSA, and incubated for 1 h at room temperature. The sample was then washed overnight in PBS.

The day after staining, the coverslip was mounted with a dSTORM buffer composed of 10% (v/v) glycerol in water with 0.1 M MEA-HCl (M6500; Sigma-Aldrich), 0.8 g/l glucose oxidase (G0543; Sigma-Aldrich), 0.220 mg/l catalase (C100; Sigma-Aldrich), 10% (w/v) glucose, 2.5 mM KCl, 2 mM Tris-HCl, and 0.4 mM TCEP (C4706; Sigma-Aldrich). The pH was adjusted to 8 with NaOH.

For capsules, before mounting, we carried out a 10-min incubation step with poly-D-lysine (Sigma-Aldrich) diluted in PBS to ensure proper attachment of the tissue to the coverslip.

**Reporting Summary.** Further information on experimental design is available in the Nature Research Reporting Summary.

**Data availability.** The data that support the findings of this study are available from the corresponding author upon reasonable request. The software is freely available for academic use and is provided with this paper as Supplementary Software.

## References

- Bon, P. et al. Three-dimensional nanometre localization of nanoparticles to enhance super-resolution microscopy. *Nat. Commun.* **6**, 7764 (2015).
- Bon, P., Lécart, S., Fort, E. & Lévêque-Fort, S. Fast label-free cytoskeletal network imaging in living mammalian cells. *Biophys. J.* **106**, 1588–1595 (2014).
- Sage, D. et al. Quantitative evaluation of software packages for single-molecule localization microscopy. *Nat. Methods* **12**, 717–724 (2015).
- Alessandri, K. et al. A 3D printed microfluidic device for production of functionalized hydrogel microcapsules for culture and differentiation of human neuronal stem cells (hNSC). *Lab Chip* **16**, 1593–1604 (2016).
- Xu, K., Babcock, H. P. & Zhuang, X. Dual-objective STORM reveals three-dimensional filament organization in the actin cytoskeleton. *Nat. Methods* **9**, 185–188 (2012).